Showcasing research from Prof. Hirotomo Nishihara's group, Tohoku University, Japan, collaborated with Prof. Fumito Tani's group, Kyushu University, Japan; Prof. Tomoki Ogoshi's group, Kyoto University, Japan; Prof. Kazuhide Kamiya's group, Osaka University, Japan.

Rational bottom-up synthesis of sulphur-rich porous carbons for single-atomic platinum catalyst supports

The bottom-up fabrication approach for sulphur(S)-rich porous carbons from molecular precursors *via* thermal polymerization process has been demonstrated. The abundant S species in the resulting carbonaceous materials function as an effective anchoring site for single-atomic platinum (Pt) species. The single-atomic Pt catalysts show the high catalytic activity for electrochemical hydrogen oxidation reaction, equivalent to commercial Pt/C catalysts, despite the significantly low Pt loading amount.

As featured in:

See Takeharu Yoshii, Tomoki Ogoshi, Kazuhide Kamiya *et al.*, *Green Chem.*, 2024, **26**, 8758.

ROYAL SOCIETY OF CHEMISTRY

rsc.li/greenchem

Registered charity number: 207890

Green Chemistry

PAPER

View Article Online
View Journal | View Issue

Cite this: *Green Chem.*, 2024, **26**, 8758

Rational bottom-up synthesis of sulphur-rich porous carbons for single-atomic platinum catalyst supports†

Koki Chida, [a] Takeharu Yoshii, *[a] Ryo Kawaguchi,[a] Masataka Inoue,[b] Fumito Tani, [b] Tatsuki Sobue,[c] Shunsuke Ohtani, [c] Kenichi Kato, [c] Tomoki Ogoshi,*[c,d] Shoko Nakahata,[e] Kazuhide Kamiya *[e,f] and Hirotomo Nishihara [a,g]

Single-atomic metal catalysts are attractive for green chemistry in terms of their outstanding catalytic performance and savings in precious metal usage owing to maximized metal utilization, including anode catalysts in polymer electrolyte fuel cells (PEFCs). Heteroatom-doped porous carbons are extensively used as supports, where the heteroatoms contribute to the immobilization of single-atomic metals. However, high-content doping of heteroatoms, especially sulphur (S), into carbon supports is still challenging because S species can be readily desorbed during heat treatment. Herein, we present a bottom-up fabrication approach for S-rich porous carbons from molecular precursors *via* a thermal polymerization process. A simple carbonization of molecules with thermally stable S-containing building blocks and polymerizable ethynyl moieties at 900 °C yields microporous carbon materials with record-high S content (over 15 wt%). The abundant S species function as an effective anchoring site for single-atomic platinum (Pt) species. Toward anode catalysts in PEFCs, the prepared single-atomic Pt catalysts efficiently promote the electrochemical hydrogen oxidation reaction, whose activity is comparable to that of commercial Pt/C, despite the significantly low Pt loading amount.

Received 26th April 2024,
Accepted 27th June 2024

DOI: 10.1039/d4gc02055c

rsc.li/greenchem

1. Introduction

A variety of catalytic processes have brought significant improvements to the chemical industry.[1,2] Platinum (Pt)-based catalysts are indispensable to industry for their superior catalytic performance in a variety of reactions.[3–5] With the growing demand for rechargeable batteries toward achieving a sustainable society, Pt has recently been extensively used as a catalyst for both the anode and cathode in polymer electrolyte fuel cells (PEFCs).[6,7] However, Pt is one of the precious metals, and there are practical issues with its limited availability and high cost. Therefore, there is an urgent need to optimize catalyst design for green chemistry.[8] From this point of view, the ultimate reduction of metal sizes down to atomic dispersion, *i.e.*, single-atomic catalysts (SACs), is one of the effective strategies to significantly improve the atomic utilization efficiency for saving precious metal usage.[9] At the same time, SACs can ensure the advantages of traditional heterogeneous catalysts, such as stability and recyclability. To date, many researchers have reported single-atomic metal catalysts on a variety of support materials, including metal oxides,[10–12] zeolites,[13,14] layered materials,[15,16] and carbon materials,[17–20] for a wide range of catalytic reaction systems. Metal oxides, zeolites and layered materials are generally unsuitable for electrocatalysis due to their low electron conductivity. Porous carbon materials, on the other hand, possess outstanding advantages especially for electrocatalysis, owing to their high porosity, electrical conductivity, and chemical/thermal stability.[21]

[a]*Institute of Multidisciplinary Research for Advanced Materials, Tohoku University, 2-1-1 Katahira, Aoba-ku, Sendai, Miyagi, 980-8577, Japan. E-mail: takeharu.yoshii.b3@tohoku.ac.jp*
[b]*Institute for Materials Chemistry and Engineering, Kyushu University, 744 Motooka, Nishi-ku, Fukuoka, 819-0395, Japan*
[c]*Department of Synthetic Chemistry and Biological Chemistry, Graduate School of Engineering, Kyoto University, Nishikyo-ku, Kyoto, 615-8510, Japan. E-mail: ogoshi@sbchem.kyoto-u.ac.jp*
[d]*WPI Nano Life Science Institute (WPI-NanoLSI), Kanazawa University, Kakuma-machi, Kanazawa, Ishikawa920-1192, Japan*
[e]*Research Center for Solar Energy Chemistry, Graduate School of Engineering Science, Osaka University, 1-3 Machikaneyama, Toyonaka, Osaka560-8531, Japan. E-mail: kamiya.kazuhide.es@osaka-u.ac.jp*
[f]*Innovative Catalysis Science Division, Institute for Open and Transdisciplinary Research Initiatives (ICS-OTRI), Osaka University Suita, Osaka, 565-0871, Japan*
[g]*Advanced Institute for Materials Research (WPI-AIMR), Tohoku University, 2-1-1 Katahira, Aoba-ku, Sendai, Miyagi, 980-8577, Japan*

†Electronic supplementary information (ESI) available: Supplemental synthetic schemes, TG-DSC-MS spectra, SEM images, TEM images, PXRD patterns, pore-size distributions, molecular probe results, HOR test results, and supplemental tables. See DOI: https://doi.org/10.1039/d4gc02055c

In order to immobilize single-atomic metal species onto carbon supports, it is necessary to create "anchoring sites" like defects on the carbon surface due to the poor interaction between the metal species and the hexagonal lattice structure of graphene sheets. Heteroatom dopants, including nitrogen (N), boron (B), sulphur (S), and phosphorus (P), can coordinate single-atomic metal species, and thus, doped carbon materials are widely used as supports for SACs.[22–24] In particular, N-doped carbon materials have been intensively studied as supports for transition metal-based SACs. On the other hand, S doping is known to be more effective than N doping for single-atomic noble metal species like Pt, due to the strong bonding between Pt and S.[25] Various methods have been reported to prepare S-doped carbon materials, such as direct conversion of small organic compounds or natural products[26–28] and post-processing of carbon materials *via* chemical reactions.[29,30] There are simultaneous requirements for supports for SACs: high heteroatom content, controlled chemical structure, and developed pores. In this regard, S-doping techniques for SACs have not yet been well established.[31] Even when a large number of S species were introduced into porous carbon frameworks, the chemical state of S species could not be uniformly controlled and contained oxidized species ($-SO_x$), which would not act as anchoring sites for metal species and would be unstable during electrocatalysis. For example, transition metal-assisted carbonization of small organic compounds has been developed, allowing the fabrication of S-doped porous carbon with a high S content of 12 wt% and a controlled pore structure. However, this methodology was not able to precisely and homogeneously control the chemical structure around the S species and required a complex synthetic process.[32] Direct carbonization of precursor molecules with well-defined S species could be a promising approach, but in practice, low-temperature decomposition or evaporation of precursors leads to the production of low-S-containing carbons in low yield.[33]

We have recently revealed that the carbonization of organic molecules *via* solid-state polymerization is an effective strategy for the formation of graphene-based porous frameworks with high carbonization yields (~90 wt%).[34] Simple carbonization of metalloporphyrin crystals with polymerizable moieties yields three-dimensional (3D) carbon materials with ordered structures.[35–39] Furthermore, carbon materials with a precisely controlled pore size at the angstrom level have been successfully produced by the carbonization of 3D aromatic molecules (tetraphenylmethane and tetrabiphenylmethane) with ethynyl groups.[37] Thus, well-designed molecules possessing thermally stable building blocks and polymerizable moieties can be used as precursors to fabricate 3D microporous carbons with molecular-level design in high yields. These studies inspired the application of this bottom-up methodology to the synthesis of carbon materials doped with high concentrations of heteroatoms.

Herein, we report the synthesis of porous carbon materials with a high S content by a simple carbonization approach as a platform for single-atomic Pt species for electrocatalysis. First, design guidelines for two-dimensional (2D) precursor molecules are established towards porous carbons. We further extended our study to the synthesis of S-doped carbons from a precursor molecule possessing benzotrithiophene units with ethynyl moieties. The ethynyl moieties are cross-linked with each other to produce rigid frameworks during heat treatment, offering a high S content (>15 wt%) and a specific surface area (>700 m^2 g^{-1}) with high carbonization yields (>59 wt%). Furthermore, single-atomic Pt species can be coordinated to S-dopants in carbon. Interestingly, the prepared single-atomic Pt catalysts show high catalytic activity equivalent to that of commercial Pt/C for the electrochemical hydrogen oxidation reaction (HOR), in spite of a significantly lower Pt content, with high durability and low side reaction activity.

Takeharu Yoshii

Takeharu Yoshii (b. 1992) received his Ph.D. degree in Engineering from Osaka University under the supervision of Professor Hiromi Yamashita in 2020. Since 2020, he has been an Assistant Professor at the Institute of Multidisciplinary Research for Advanced Materials (IMRAM), Tohoku University, working with Professor Hirotomo Nishihara. He was conferred the title of Prominent Research Fellow at Tohoku University in 2023. From 2023 to the present, he has been participating in the JST PREST "Future Materials" program. His work focusses on the design and synthesis of nanostructured heterogeneous catalysts, especially carbon-based single-atomic metal catalysts for green chemistry.

2. Experimental

Chemicals

Reagents and solvents of the best grade available were purchased from commercial suppliers and were used without further purification unless otherwise noted.

Synthesis

Pyrene (**1**) was obtained commercially (Wako Pure Chemical Industries, Ltd). 1-Ethynylpyrene (**2**) was synthesized according to the previous work (see Scheme S1a†).[40,41]

^{1}H NMR (400 MHz, $CDCl_3$): 8.60 (d, J = 9.2 Hz, 1H), 8.24 (d, J = 8.4 Hz, 1H), 8.22 (d, J = 8.4 Hz, 1H), 8.19 (d, J = 9.2 Hz, 1H), 8.18 (d, J = 8.0 Hz, 1H), 8.12 (d, J = 8.0 Hz, 2H), 8.06 (d, J = 8.8 Hz, 1H), 8.04 (t, J = 7.6 Hz, 1H), 3.63 (s, 1H).

A pyrene-based molecule with four ethynyl moieties (1,3,6,8-tetraethynylpyrene, **3**) was synthesized according to the previous work (see Scheme S1b†).[42]

^{1}H NMR (400 MHz, $CDCl_3$): δ 3.67 (s, 4H), 8.49 (s, 2H), 8.69 (s, 4H).

A molecule with a thiophene skeleton and ethynyl moieties (2,5,8-tri(triethynyl)benzo[1,2-*b*:3,4-*b*:5,6-*b*″]-trithiophene, **1S**) was obtained according to previous work (see Scheme S2†).[43,44]

^{1}H NMR (400 MHz, $CDCl_3$): δ 3.52 (s, 3H), 7.73 (s, 3H).

Benzotrithiophene (**2S**) was obtained commercially (Wako Pure Chemical Industries, Ltd).

Heat treatment of the samples was conducted under a N_2 flow in a tubular furnace by using a temperature heating program as shown in Scheme S3.† The heat-treated samples are denoted as *X*_*T*, where *X* indicates the type of precursor (**2**, **3** and **1S**) and *T* is the heat treatment temperature (700 or 900 °C).

Characterization

^{1}H NMR spectra were recorded at 400 MHz using a JNM-ECS400 spectrometer (Jeol Resonance Inc.). ^{1}H chemical shifts were expressed as values relative to tetramethylsilane (TMS). The thermal decomposition behaviours of the precursors were assessed by simultaneous analysis systems including thermogravimetry, differential scanning calorimetry, and mass spectroscopy (TG-DSC-MS). TG-DSC was conducted on a STA 449 Jupiter (Netzsch) from 60 °C to 900 °C at a heating rate of 10 °C min^{-1} under a He flow (150 mL min^{-1}). The emission gas from TG-DSC was analysed by using a quadrupole mass spectrometer (JMS-Q1500GC, JEOL). Scanning electron microscopy (SEM) images were obtained on a FE-SEM using a Hitachi-S4800. Powder XRD (PXRD) patterns for all the samples were collected using a MiniFlexII (Rigaku Co., Tokyo, Japan) between 2 and 40° (2θ) with a 0.01° step (conditions: Cu-Kα radiation, 45 kV, 15 mA, 1.5418 Å). Transmission electron microscopy (TEM) images of the carbonized samples were obtained using a JEOL JEM-2010 operated at 100 kV. Raman spectra were obtained on a LabRAM HR resolution spectrometer (HORIBA) with a laser wavelength of 532 nm, and the intensity was normalized by the G-band. X-ray photoelectron spectroscopy (XPS) analysis was performed using a JEOL JPS-9200 (Al-Kα radiation) for S 2p spectra and a Kratos Analytical Co. Axis Ultra (Al-Kα radiation) for Pt 4f spectra. For analysis, the binding energy of a peak corresponding to sp^2 carbon was calibrated to 284.5 eV.[45] Elemental analysis was conducted using a MICRO CORDER JM10 and JM S (J-Science Lab. Inc.). N_2 adsorption and desorption isotherms were obtained using a BELSORP-max system (MicrotracBEL Corp.) and QUADRASORB EVO4 (Quantachrome Instruments) at −196 °C. The Brunauer–Emmett–Teller (BET) surface area (S_{BET}) was calculated using the multipoint BET method from the adsorption data in the range of P/P_0 = 0.01–0.05.[46] The pore size distribution was calculated with the non-local density functional theory (NLDFT) using a slit-pore model.[47] Adsorption with various molecular probes was measured using a BELSORP-max system (MicrotracBEL Corp.) at 25 °C. Molecular probes of different kinetic diameters, including CO_2 (0.33 nm at 25 °C), ethane (0.40 nm at 25 °C), *n*-butane (0.43 nm at 25 °C), *n*-hexane (0.49 nm at 25 °C), and tetrachloromethane (0.60 nm at 25 °C), were used for adsorption to evaluate the pore size of the adsorbents.[37,48,49] Pt L_3-edge X-ray absorption fine structure (XAFS) spectra were recorded in transmission mode by synchrotron radiation at the Beamline BL01B1 in SPring-8, JASRI, Harima, Japan, using an Si (111) monochromator. Fourier transform was applied to the k^3-weighted normalized extended X-ray absorption fine structure (EXAFS) data over the range of $3.0 < k$ (Å^{-1}) < 12 to obtain radial structure functions using Athena and Artemis.[50] Curve fitting analysis for EXAFS spectra was performed using a *quick first shell* offered by Artemis. The coordination number of Pt-S and Pt-Cl bonding for *cis*-[Pt(DMSO)$_2$Cl$_2$] was fixed to 2 to determine S_0^2: backscattering amplitude factor. Then, the calculated S_0^2 was also employed for the curve fitting analysis of Pt-**1S**_900. Wavelet transform analysis of EXAFS was conducted using the Morlet function as a mother wavelet.[51]

Electrochemical hydrogen oxidation reaction performance

For the preparation of working electrodes, 1.0 mg of **3**_900 or **1S**_900 was mixed with 5 wt% Nafion™ solution (20 μL) and ethanol (300 μL), and then, the suspension was sonicated. For **1S**_900, 80 μL of catalyst ink was dropped onto a 0.125 cm^2 polished rotating disk electrode (RDE) with a catalyst loading of 2.0 mg cm^{-2}. For **3**_900, 16 μL of catalyst ink was dropped onto a 0.125 cm^2 polished RDE with a catalyst loading of 0.4 mg cm^{-2}. For an impregnation process of Pt species, the as-prepared working electrodes of **1S**_900 or **3**_900 were immersed in an aqueous solution of 10 mM $K_2[PtCl_4]$ and rotated for 5 h, and then washed with deionized water to prepare Pt-modified catalysts (denoted as Pt-**1S**_900 and Pt-**3**_900, respectively). As a reference catalyst, commercial 20 wt% Pt/C (HiSPEC3000, Johnson Matthey) was used. The catalyst ink of Pt/C was prepared by the same method described above. Then, the as-prepared catalyst ink of 20 wt% Pt/C was dropped onto a 0.125 cm^2 polished RDE with a catalyst loading of 2.0 mg cm^{-2}. The electrocatalytic hydrogen oxidation reaction (HOR) performance was evaluated at room temperature by the RDE method at a rotation rate of 2500 rpm in 0.1 M $HClO_4$ aq. (pH: 1.0) under a H_2 flow (10 sccm). A saturated Ag/AgCl electrode and a glassy carbon electrode were used as the reference and counter electrodes, respectively. The potential [*V*] was converted from Ag/AgCl to the reversible hydrogen electrode (RHE) scale using the following equation (eqn (1)).

$$\text{Potential (RHE)} = \text{potential (Ag/AgCl)} + 0.059 \times \text{pH} + 0.1967 \quad (1)$$

Linear sweep voltammetry (LSV) was evaluated between 0 and 0.4 V *vs.* RHE with a scan rate of 2 mV sec^{-1} in Ar or H_2 saturated 0.1 M $HClO_4$ aq. (pH: 1.0). The oxygen reduction reaction (ORR) activity was also measured by LSV between 0.2 and 1.2 V *vs.* RHE with a scan rate of 2 mV sec^{-1} at a rotation rate of 2500 rpm in 0.1 M $HClO_4$ aq. (pH: 1.0) under an O_2 flow (10 sccm).

3. Results and discussion

Synthesis of 3D porous carbon from 2D precursor molecules

To prepare design guidelines for precursors towards 3D porous carbon materials, three types of pyrene-based molecules with or without ethynyl moieties (**1**–**3**) were investigated (see Fig. 1). The thermal behaviours of these precursors were first examined using TG-DSC-MS (Fig. 1a–c and Fig. S1†). **1** evaporates when the temperature reaches 300 °C, with endothermic DSC peaks and the corresponding MS spectrum of **1** itself. In contrast, **2** and **3** molecules exhibit exothermic DSC peaks at around 160 °C, which correspond to the thermal polymerization of ethynyl moieties. The thermal decomposition of **2** and **3** molecules is significantly prevented, thanks to the polymerization, and the resulting yields at 900 °C are 45 wt% and 78 wt% in the case of **2** and **3**, respectively. Based on these thermal analyses, **2** and **3** were employed as carbon precursors, carbonized at 900 °C under an N_2 atmosphere, and the resulting materials are denoted as **2**_900 and **3**_900, respectively. As shown in the photos in Fig. S2a and S2b,† molecule **2** has largely changed its powder shape during the carbonization process, while molecule **3** is carbonized while maintaining the shape. Moreover, SEM observation revealed that the morphology of **3** at the μm level is retained well even after the carbonization at 900 °C (Fig. S2c and S2d†), unlike the case of **2** (Fig. S2e and S2f†). Here, the TG-DSC profile for precursor **2** (see Fig. 1b) shows a sharp endothermic peak without weight loss at around 120 °C, which is attributed to the melting of the molecule before polymerization. On the other hand, no melting-derived peak can be observed for precursor **3** (see Fig. 1c). Thus, precursor **2** changed its morphology due to carbonization *via* melting, while precursor **3** underwent solid-state polymerization and subsequent carbonization. These results show that introducing multiple polymerizable moieties into aromatic units can avoid their melting and evaporation process, allowing morphology-preserved carbonization *via* polymerization. From PXRD patterns (Fig. S3†), both crystalline structures of precursors are converted to amorphous structures after the carbonization process. A diffraction peak at around 25° of **2**_900 can be assigned to carbon (002), *i.e.*, graphene stacking structures. In the case of **3**_900, the (002) peak is broader and weaker than that of **2**_900, suggesting that the graphene stacking is not well developed, probably due to the formation of 3D graphene frameworks by carbonization *via* solid-state polymerization. Raman spectra of **2**_900 and **3**_900 (Fig. 1d) exhibit D- and G-bands at 1355 and 1590 cm^{-1}, respectively, indicating the formation of defective carbon structures.[52] The I_D/I_G ratios of **2**_900 and **3**_900 are calculated to be 0.92 and 1.0, respectively (Table S1†), suggesting no significant difference in the quality of the obtained carbon materials. However, porous texture properties are quite different from each other. N_2 adsorption/desorption isotherms of a series of **2** and **3** are summarized in Fig. 1e and f, respectively. Both precursors **2** and **3** are poorly porous (S_{BET}: 1 and 24 $m^2\ g^{-1}$,

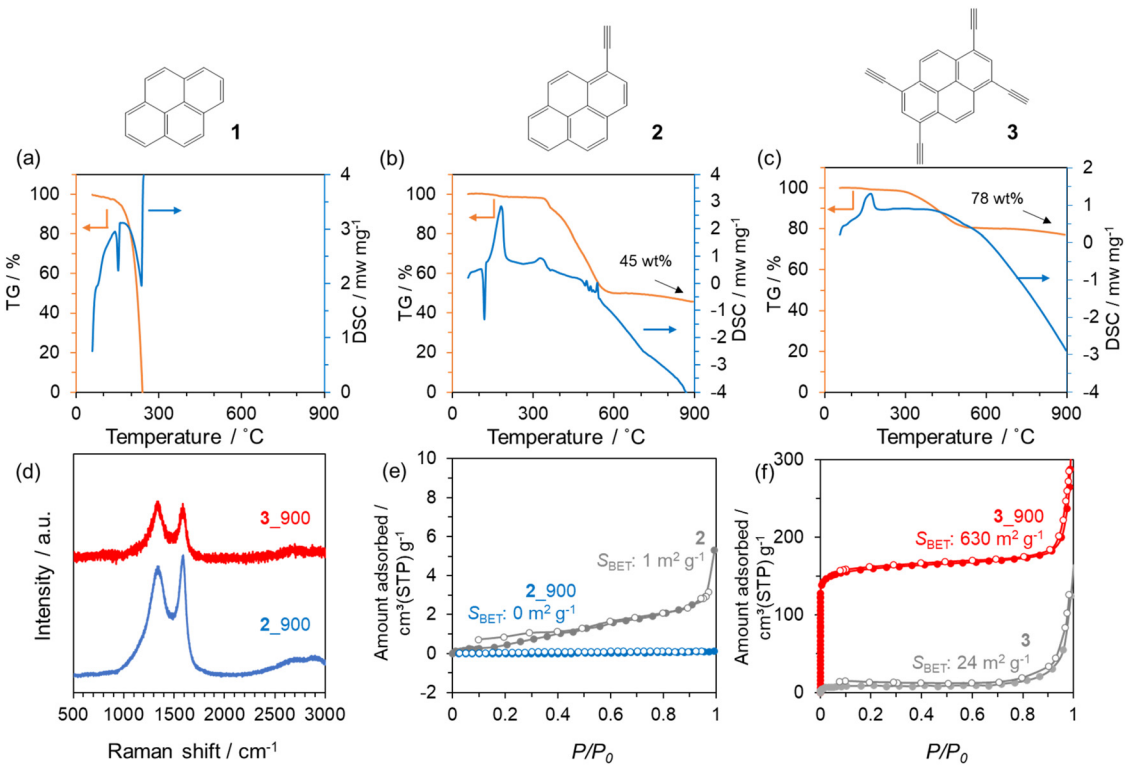

Fig. 1 TG-DSC profiles of (a) **1**, (b) **2** and (c) **3**. (d) Raman spectra of **2**_900 and **3**_900. N_2 adsorption/desorption isotherms of (e) **2** and **2**_900, and (f) **3** and **3**_900.

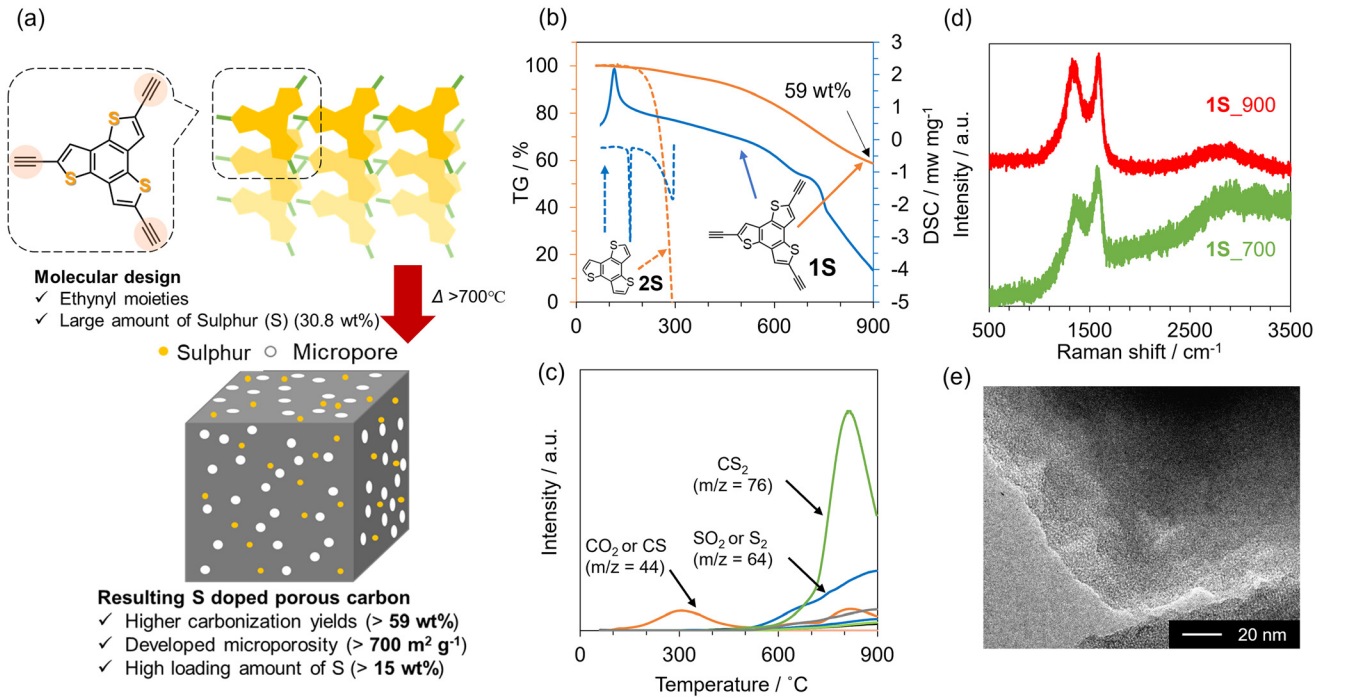

Fig. 2 (a) Molecular design of the precursor and the schematic synthetic strategy for highly S-doped porous carbons. (b) TG-DSC profiles for **1S** (solid lines) and **2S** (dashed lines) and (c) the corresponding MS spectra for **1S**. (d) Raman spectra of **1S**_700 and **1S**_900. (e) TEM image of **1S**_900.

respectively). **2**_900 also shows a non-porous structure even after carbonization (S_{BET}: 0 m^2 g^{-1}). On the other hand, the microporous structure is well developed through the carbonization process in the case of **3**, and **3**_900 exhibits an S_{BET} of 630 m^2 g^{-1}. Taking these characterization results into consideration, introducing multiple ethynyl moieties into 2D aromatic compounds enables the prevention of the liquid-phase transition during heat treatment, but also allows carbonization *via* solid-state polymerization, resulting in the formation of microporous carbon materials.

Synthesis of sulphur-doped 3D porous carbon

We then aimed to synthesize highly S-doped porous carbon materials on the basis of the above-suggested design guidelines. Fig. 2a schematically illustrates the preparation of 3D S-doped carbon in this study. Firstly, the precursor molecule (**1S**), including the thiophene skeleton and multiple ethynyl moieties, was synthesized according to the previous work (see also Scheme S2†).[43,44] Then, we investigated the thermal behaviour of **1S** using TG-DSC-MS as shown in Fig. 2b and c. As a control sample, commercial benzotrithiophene (denoted as **2S**) with no polymerizable moieties was employed. While **2S** completely disappears at around 300 °C, **1S** demonstrates a high carbonization yield (59 wt%) even after carbonization at 900 °C, exceeding that of previous works (typically less than 40 wt% over 700 °C).[53,54] Additionally, an intense exothermic peak can be observed at around 120 °C for **1S**, suggesting that ethynyl moieties in **1S** are thermally polymerized with each other. Alternatively, **2S** exhibits endothermic peaks at around 150 °C and 300 °C, which correspond to its melting and gasification processes, respectively. The MS spectra for **1S** show a small amount of desorbed gas species (CO_2 or CS, m/z = 44) up to 300 °C (Fig. 2c), while **2S** exhibits only m/z = 246, derived from the precursor itself (Fig. S4†). These thermal analyses clearly indicate that ethynyl moieties avoid the gasification of the precursor *via* the formation of cross-linked frameworks, subsequently yielding a carbon material with high yield. When the temperature reaches 600 °C, sulphur-containing gas species are gradually desorbed including CS_2 and SO_2 from **1S**. It should be noted that SO_2 and CO_2 were probably generated by reactions with the contaminated air during the TG-DSC-MS measurements, which are unavoidable in this system. Based on these results, S-doped carbon materials were prepared by the carbonization of **1S** at 700 or 900 °C under a N_2 atmosphere, according to Scheme S3,† and the as-prepared samples are denoted as **1S**_700 and **1S**_900, respectively. The PXRD pattern of **1S** exhibits some peaks corresponding to its crystalline structure (Fig. S5†). These sharp peaks disappear after the carbonization process, indicating its conversion to an amorphous structure. Raman spectra of **1S**_700 and **1S**_900 (Fig. 2d) demonstrate D- and G-bands at 1355 and 1590 cm^{-1}, respectively, indicating the formation of defective carbons, similar to **2**_900 and **3**_900 (see Fig. 2d and Table S1†).[52] TEM images of carbonized **1S** samples (Fig. 2e and S6†) show no graphene stacking structures but numerous micropores as a bright contrast.

To investigate the chemical nature of **1S** and carbonized samples, XPS analysis was performed. In the S 2p XPS spectra

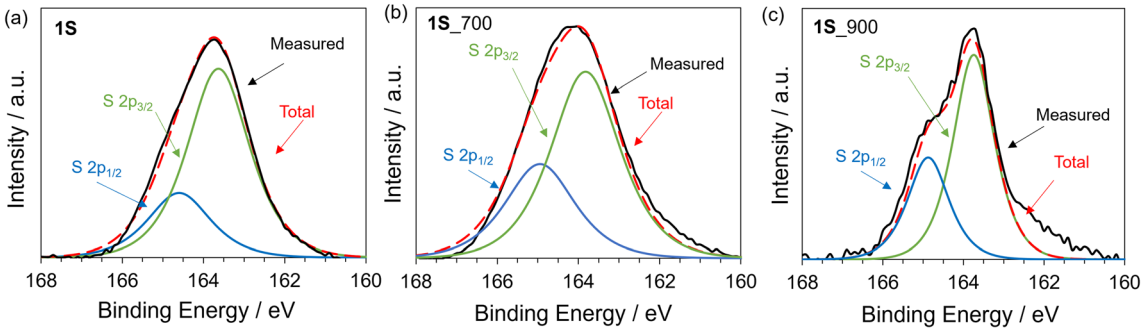

Fig. 3 S 2p XPS spectra of (a) **1S**, (b) **1S**_700, and (c) **1S**_900.

of **1S** (Fig. 3a), the S $2p_{1/2}$ and S $2p_{3/2}$ orbitals are observed at 164.5 eV and 163.5 eV, respectively. These peaks can be assigned to thiophene-type S.[55,56] In the case of **1S**_700 and **1S**_900 samples, S $2p_{1/2}$ and S $2p_{3/2}$ peaks are also observed at similar binding energies for **1S** (Fig. 3b and c), with the absence of the oxidized S species at around 168 eV.[57] Previous works have reported that the carbonization of organic molecules or polymers including thiophene-type S species yielded S-doped carbon materials possessing oxidized S and thiophene-type S species.[28,58] Thus, the heat treatment of precursor **1S** *via* solid-state polymerization would contribute to the retention of thiophene-type S species even after carbonization up to 900 °C. Furthermore, the S content of **1S**_700 and **1S**_900 is as high as 19.9 and 15.6 wt%, respectively, as determined from the elemental analysis (Table S2†). The sulphur content of the precursor molecule (**1S**) is calculated to be 30.8 wt% based on the molecular formula. Thus, the yield of sulphur is more than 50% in the whole process even after the carbonization process at 900 °C.

N_2 adsorption/desorption isotherms of a series of carbonized **1S** samples are summarized in Fig. 4a. The precursor **1S** is almost non-porous, but the carbonized samples exhibit a clear type-I isotherm, indicating the development of a microporous structure. Indeed, **1S**_700 and **1S**_900 exhibit high S_{BET} of 714 and 795 $m^2\ g^{-1}$, respectively (Table S3†). Pore-size distributions from the NLDFT analysis suggest the formation of a micropore less than 1 nm (Fig. S7†). Thus, the molecular probe method was applied to estimate the pore size more accurately, revealing that a pore of 4.8 Å is formed in **1S**_900 (Fig. 4b and S8†). In Fig. 4c and d, we compare the sulphur contents and S_{BET} values of **1S**_700 and **1S**_900 with the previously reported S-doped carbon materials prepared at 700 or 900 °C (see also Table S4†).[27,28,59–67] Interestingly, S-doped carbons synthesized in this work achieve a well-balanced porosity and sulphur content; especially, the highest S content is attained after the heat treatment at 900 °C while maintaining a high specific surface area. Therefore, the precursor design of **1S**, with thiophene-type S species and ethynyl moieties, provides multiple benefits, including high carbonization yields, high S contents and high porosity in the resulting carbons.

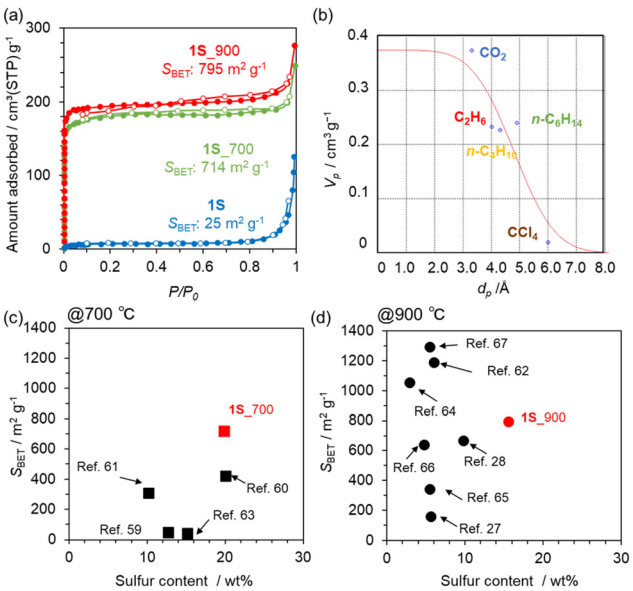

Fig. 4 (a) N_2 adsorption/desorption isotherms of **1S**, **1S**_700, and **1S**_900 samples. (b) Micropore volume (V_p) of **1S**_900 estimated by the Dubinin–Astakhov method, plotted against the kinetic diameter (d_p) of molecular probes. Comparison plots of sulphur content and the S_{BET} of S-doped carbons prepared at (c) 700 °C and (d) 900 °C in previous reports and in this work.

Application for single-atomic platinum catalyst supports

We applied the S-doped porous carbons for an electrochemical catalyst support, as sulphur species has lone electron pairs which could be coordinated with metal species. **1S**_900 was employed as the catalyst support here in terms of electrical conductivity, and Pt loading was carried out according to a previous work.[68] The as-prepared sample is denoted as Pt-**1S**_900. Pt modification was also executed using **3**_900, microporous carbon without S species (denoted as Pt-**3**_900). Fig. 5a shows the Pt 4f XPS spectra of both Pt-modified samples. The loading amounts of Pt species on Pt-**1S**_900 and Pt-**3**_900 are determined to be 0.7 and 0.1 wt%, respectively, from XPS analysis (Table S5†). Since the specific surface areas of both samples are not much different (see Table S3†), the large

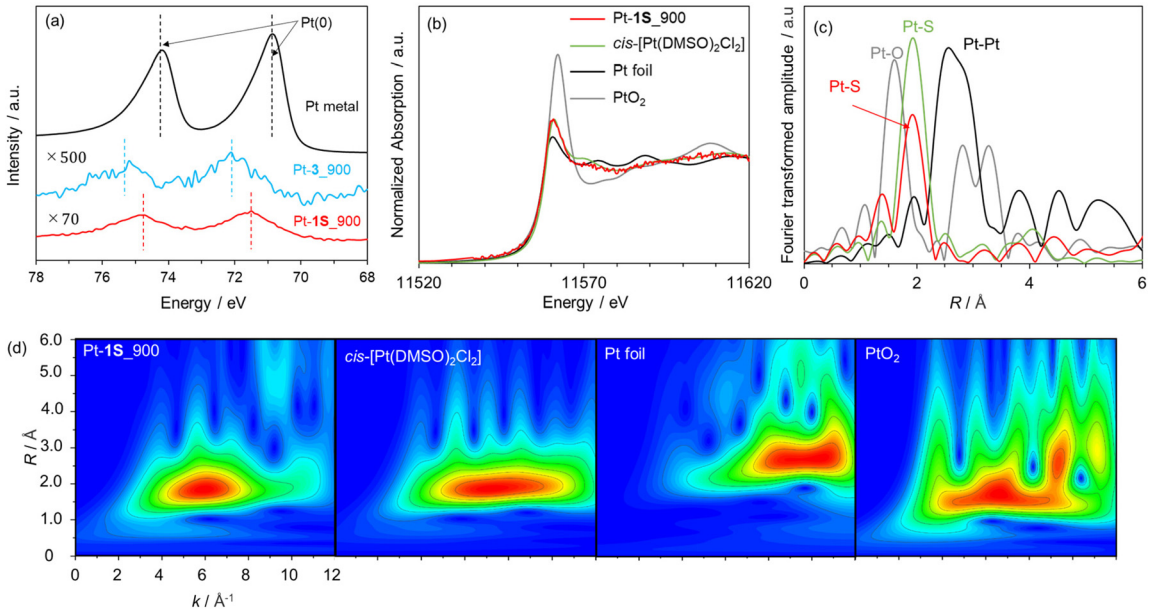

Fig. 5 (a) Pt 4f XPS spectra of Pt-**1S**_900, Pt-**3**_900, and Pt metal. (b) Pt L_3-edge XANES spectra and (c) Fourier transforms of k^3-weighted EXAFS oscillations for Pt-**1S**_900, *cis*-[Pt(DMSO)$_2$Cl$_2$], Pt foil, and PtO_2. (d) Wavelet transforms of Pt-**1S**_900, *cis*-[Pt(DMSO)$_2$Cl$_2$], Pt foil, and PtO_2.

difference in Pt loading strongly suggests that the S species in **1S**_900 contribute to the immobilization of Pt metal species. In addition, Pt-**1S**_900 has a higher binding energy than the Pt metal in the Pt 4f spectra, indicating the oxidized state of Pt species. Previous works have revealed that the oxidation state of atomically dispersed Pt species generally fluctuates from 2^+ to 4^+, due to interactions between Pt atoms and catalyst supports.[69,70] In order to examine the local structure of Pt species, Pt L_3-edge XAFS analysis was carried out. In the XANES spectra (Fig. 5b), the intensity of the white line edge of Pt-**1S**_900 is identical to that of the *cis*-[Pt(DMSO)$_2$Cl$_2$] reference, indicating that the oxidation state of Pt is divalent in Pt-**1S**_900.[69] Fourier transforms of the EXAFS spectra of Pt foil and PtO_2 show distinct peaks corresponding to Pt–Pt and Pt–O bonding at 2.55 and 1.60 Å, respectively (Fig. 5c). In clear contrast, Pt-**1S**_900 exhibits a peak at 1.96 Å, which is consistent with the *cis*-[Pt(DMSO)$_2$Cl$_2$] reference, being ascribed to Pt–S or Pt–Cl bonding. In addition, Pt–Pt bonding is not detected in Pt-**1S**_900, demonstrating that Pt species dominantly present as atomically dispersed Pt atoms coordinated with S species. Further quantitative analysis of the coordination structure was carried out by fitting the *R*-space of Pt-**1S**_900 with Pt–S and Pt–Cl bonding (Table 1). The coordination numbers of Pt–S and Pt–Cl bonding in the first coordination shell of Pt-**1S**_900 are estimated to be 2.6 and 2.4, respectively, which are close to those for *cis*-[Pt(DMSO)$_2$Cl$_2$]. This fitting result implies that the coordination structure of Pt species in Pt-**1S**_900 is similar to that of the Pt(II) complex. To further unveil the local environment of Pt species, we performed wavelet transform (WT) analysis (Fig. 5d), which allows a resolution of the back-scattering atoms in both *k*- and *R*-spaces.[71] The WT of EXAFS signals for Pt foil indicate a single intensity maximum at around 9.3 $Å^{-1}$ due to the Pt–Pt contribution. In contrast, the WT of EXAFS shows an intensity maximum at around 6 $Å^{-1}$ for Pt-**1S**_900, *cis*-[Pt(DMSO)$_2$Cl$_2$], and PtO_2, which can be assigned to the Pt–S/O contribution of the first nearest-neighbour coordination shell. The similarity between the Pt coordination of Pt-**1S**_900 and *cis*-[Pt(DMSO)$_2$Cl$_2$] can also be clearly recognized from WT. Combining the FT and WT of EXAFS analysis, it can be concluded that the Pt species in Pt-**1S**_900 are atomically dispersed in the divalent state coordinated to the S species, without aggregation into particles.

The electrocatalytic performance of Pt-**1S**_900 for the hydrogen oxidation reaction (HOR) was evaluated by linear sweep voltammetry (LSV) in H_2 saturated 0.1 M $HClO_4$ aq. Commercial Pt/C and Pt-**3**_900 were employed as control

Table 1 Structural parameters calculated from the EXAFS fitting results of Pt-**1S**_900

Sample	Shell	Coordination number	*R*/Å	e^0/eV	σ^a/Å	*R*-factor/%
cis-[Pt(DMSO)$_2$Cl$_2$]	Pt-S	2[b]	2.31	14.3	0.048	0.8
	Pt-Cl	2[b]	2.30	13.9	0.053	0.8
Pt-**1S**_900	Pt-S	2.6	2.30	11.4	0.10	0.1
	Pt-Cl	2.4	2.28	11.9	0.10	0.1

[a] Debye–Waller factor. [b] Fixed.

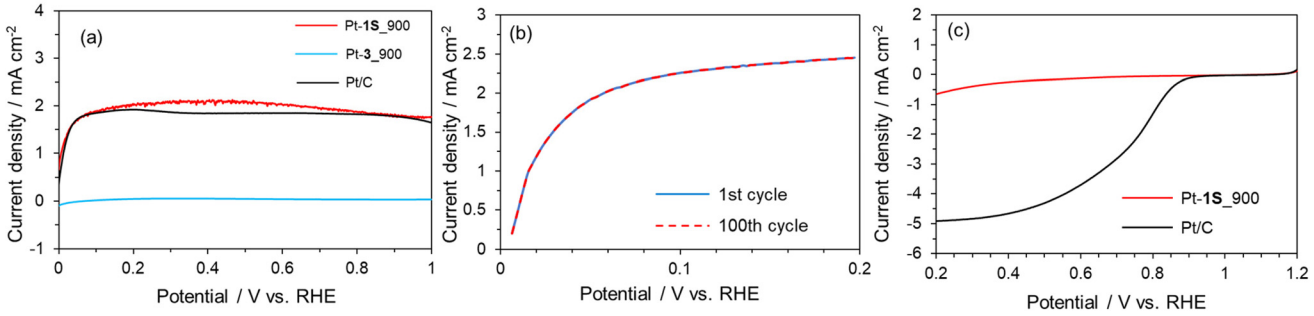

Fig. 6 (a) Polarization curves for the HOR of Pt-**1S**_900, Pt-**3**_900 and Pt/C under a H_2 flow. (b) Polarization curves for the HOR of Pt-**1S**_900 for the 1st and 100th cycle. (c) Polarization curves for the ORR of Pt-**1S**_900 and Pt/C.

samples. Under Ar-saturated conditions, none of the catalysts (Pt-**1S**_900, Pt-**3**_900, and Pt/C) exhibit faradaic current (Fig. S9†). In contrast, **1S**_900 displays a clear increase in current from 0 V *vs.* RHE (namely, without overpotential) under the H_2-saturated conditions, similar to Pt/C (Fig. 6a). No faradaic current can be observed in Pt-**3**_900, probably due to a much smaller loading amount or an overoxidized state of Pt species compared to **1S**_900 (see Fig. 5a and Table S5†). These results reveal that single-atomic Pt species supported on S-doped carbon function as an efficient electrocatalyst for the HOR. Notably, Pt-**1S**_900 shows catalytic activity equivalent to Pt/C, in spite of a much lower Pt loading amount (less than one-twelfth, see Table S5†). Such high catalytic performance could be attributed to the higher atom utilization efficiency of atomically dispersed Pt species. Furthermore, there was no significant change in the Pt content of Pt-**1S**_900 before and after the electrochemical test, demonstrating no leaching of Pt species even under acidic conditions (Table S5†). The stability test was carried out by LSV for 100 cycles (Fig. 6b). The high catalytic activity of Pt-**1S**_900 was well retained even after 100 cycles, further indicating the durability of S-coordinated Pt species for the electrochemical HOR. When considering its practical application in PEFCs, air contamination inevitably happens in the anode chamber during the start-up of PEFCs, and the cathodic oxygen reduction reaction (ORR) occurs as a side reaction on the Pt anode catalysts. This phenomenon induces a decrease in power generation and the deterioration of carbon supports. Thus, we further investigated the electrocatalytic ORR activity. Fig. 6c shows the polarization curves of Pt-**1S**_900 and Pt/C for the ORR. The current density of Pt-**1S**_900 is significantly smaller compared to Pt/C, indicating its extremely low catalytic activity for the ORR. Therefore, single-atomic Pt coordinated to S-doped carbons can be regarded as one of the ideal anode catalysts for PEFCs in terms of activity per Pt amount, durability, and low ORR reactivity.

4. Conclusions

In summary, we have initially established the guidelines for an efficient bottom-up preparation of 3D porous carbon materials; molecular precursors with multiple polymerizable ethynyl groups are converted to microporous carbons in high yields *via* solid-state polymerization. According to the guidelines, we have also succeeded in the fabrication of S-rich porous carbons from the simple carbonization of the precursor molecule including the thiophene skeleton and ethynyl moieties. Notably, this work achieved a high content (over 15 wt%) of sulphur species with a homogeneous chemical structure in well-developed microporous carbons, even after carbonization at as high as 900 °C. This can be attributed to the formation of rigid 3D cross-linked frameworks by ethynyl moieties, suppressing the decomposition during the carbonization process. We further applied the prepared S-rich porous carbon materials as supports for single-atomic Pt species. High catalytic activity for the electrochemical HOR is demonstrated, equivalent to that of commercial Pt/C, in spite of a much smaller Pt loading amount. Moreover, Pt coordinated S-doped carbons show high long-term stability and low catalytic activity for a side reaction of the ORR, suggesting suitable catalytic performance for their practical application in PEFC anodes.

From the perspective of green chemistry, the HOR, the target of this study, is a green catalytic process. However, the use of organic solvents, including toluene, $CHCl_3$, TEA, THF, and NMP, is unavoidable in the organic synthesis of precursor molecules for catalyst supports, although only for temporary use during catalyst synthesis. Future developments in green organic chemistry, such as solid-state cross-coupling reactions, are expected to reduce the use of organic solvents. With regard to recyclability, the prepared catalysts consist of C, H, S, and Pt species. C, H, and S are abundant resources, but the recovery of Pt species from the catalyst is crucial. Here, C, H and S are combustible, so Pt species can be recovered by burning the catalyst after use, as is the case with conventional Pt/C catalysts. In terms of saving in Pt usage, reducing the Pt amount in cathode catalysts is also an urgent issue in PEFCs, since cathode catalysts require more Pt than anode catalysts. However, the prepared single-atomic Pt catalysts are active for the HOR but inactive for the ORR. Therefore, unfortunately, this methodology cannot contribute to the reduction of Pt usage in cathode sides at this stage. The synthetic approach for highly S-doped carbon materials presented in this study is

expected to be extended to diverse heteroatom systems such as N, B and P. For example, highly N-doped carbons can be used in single-atomic transition metal catalyst supports, opening up to a variety of reaction systems such as the ORR and CO_2 conversion. Therefore, the present rational design for highly hetero-doped porous carbons provides potential applications toward various catalytic systems that are important for green chemistry.

Data availability

All data supporting the findings of this study are available within the article and its ESI† file.

Author contributions

Investigation: K. C., R. K., T. F., T. S. and S. N.; formal analysis: K. C., R. K., T. S. and S. N.; supervision: T. Y., S. O., K. Kato, T. O., K. Kamiya and H. N.; project administration: T. Y., T. O., K. Kamiya and H. N.; writing – original draft: K. C.; writing – review & editing: T. Y. and H. N. All authors have given approval to the final version of the manuscript.

Conflicts of interest

There are no conflicts to declare.

Acknowledgements

This work was supported by JST CREST Grant no. JPMJCR18R3; JSPS KAKENHI Grant no. 23H02063, 21K14490 and 22KJ0294; the "Five-star Alliance" in "NJRC Mater. & Dev."; and JST SICORP Grant no. JPMJSC2112. The authors thank Prof. R. Sakamoto and Prof. Y. Nishina for precious discussions and Dr N. Hashimoto for the support toward XAFS analysis. The XAFS experiments using synchrotron radiation were performed at the Beamline BL01B1 in SPring-8, Harima, Japan (proposal no. 2023A1690).

References

1 C. J. M. van der Ham, M. T. M. Koper and D. G. H. Hetterscheid, *Chem. Soc. Rev.*, 2014, **43**, 5183–5191.
2 M. Stürzel, S. Mihan and R. Mülhaupt, *Chem. Rev.*, 2016, **116**, 1398–1433.
3 R. Liu, H. Wu, J. H. Shi, X. M. Xu, D. Zhao, Y. H. Ng, M. L. Zhang, S. J. Liu and H. Ding, *Catal. Sci. Technol.*, 2022, **12**, 6945–6991.
4 M. Paulis, H. Peyrard and M. Montes, *J. Catal.*, 2001, **199**, 30–40.
5 R. Buitrago-Sierra, M. J. García-Fernández, M. M. Pastor-Blas and A. Sepúlveda-Escribano, *Green Chem.*, 2013, **15**, 1981.
6 D. Banham and S. Y. Ye, *ACS Energy Lett.*, 2017, **2**, 629–638.
7 M. N. Islam, A. B. M. Basha, V. O. Kollath, A. P. Soleymani, J. Jankovic and K. Karan, *Nat. Commun.*, 2022, **13**, 6157.
8 P. Anastas and N. Eghbali, *Chem. Soc. Rev.*, 2010, **39**, 301–312.
9 X. F. Yang, A. Q. Wang, B. T. Qiao, J. Li, J. Y. Liu and T. Zhang, *Acc. Chem. Res.*, 2013, **46**, 1740–1748.
10 B. T. Qiao, A. Q. Wang, X. F. Yang, L. F. Allard, Z. Jiang, Y. T. Cui, J. Y. Liu, J. Li and T. Zhang, *Nat. Chem.*, 2011, **3**, 634–641.
11 R. Lang, X. R. Du, Y. K. Huang, X. Z. Jiang, Q. Zhang, Y. L. Guo, K. P. Liu, B. T. Qiao, A. Q. Wang and T. Zhang, *Chem. Rev.*, 2020, **120**, 11986–12043.
12 S. De, A. S. Burange and R. Luque, *Green Chem.*, 2022, **24**, 2267–2286.
13 Y. W. Liu, Z. Li, Q. Y. Yu, Y. F. Chen, Z. W. Chai, G. F. Zhao, S. J. Liu, W. C. Cheong, Y. Pan, Q. H. Zhang, L. Gu, L. R. Zheng, Y. Wang, Y. Lu, D. S. Wang, C. Chen, Q. Peng, Y. Q. Liu, L. M. Liu, J. S. Chen and Y. D. Li, *J. Am. Chem. Soc.*, 2019, **141**, 9305–9311.
14 Q. Zhang, S. Q. Gao and J. H. Yu, *Chem. Rev.*, 2023, **123**, 6039–6106.
15 T. Yoshii, K. Tamaki, Y. Kuwahara, K. Mori and H. Yamashita, *J. CO2 Util.*, 2021, **52**, 101691.
16 P. Huang, J. Huang, S. A. Pantovich, A. D. Carl, T. G. Fenton, C. A. Caputo, R. L. Grimm, A. I. Frenkel and G. Li, *J. Am. Chem. Soc.*, 2018, **140**, 16042–16047.
17 B. Marinho, M. Ghislandi, E. Tkalya, C. E. Koning and G. de With, *Powder Technol.*, 2012, **221**, 351–358.
18 K. Nakatsuka, T. Yoshii, Y. Kuwahara, K. Mori and H. Yamashita, *Phys. Chem. Chem. Phys.*, 2017, **19**, 4967–4974.
19 T. Yoshii, K. Nakatsuka, Y. Kuwahara, K. Mori and H. Yamashita, *Chem. Lett.*, 2017, **46**, 789–791.
20 S. J. Liu, L. C. Bai, A. P. van Muyden, Z. J. Huang, X. J. Cui, Z. F. Fei, X. H. Li, X. L. Hu and P. J. Dyson, *Green Chem.*, 2019, **21**, 1974–1981.
21 J. Maruyama, H. Sato, Y. Takao, S. Maruyama, S. Kato, K. Kamiya, K. Chida, T. Yoshii, H. Nishihara and F. Tani, *Nanoscale*, 2023, **15**, 9954–9963.
22 J. P. Paraknowitsch and A. Thomas, *Energy Environ. Sci.*, 2013, **6**, 2839–2855.
23 J. T. Zhang and L. M. Dai, *ACS Catal.*, 2015, **5**, 7244–7253.
24 T. Asefa and X. X. Huang, *Chem. – Eur. J.*, 2017, **23**, 10703–10713.
25 C. H. Choi, M. Kim, H. C. Kwon, S. J. Cho, S. Yun, H.-T. Kim, K. J. J. Mayrhofer, H. Kim and M. Choi, *Nat. Commun.*, 2016, **7**, 10922.
26 S. S. Desa, T. Ishii and K. Nueangnoraj, *ACS Omega*, 2021, **6**, 24902–24909.
27 G. G. Zhao, Y. Zhang, G. Q. Zou, Y. Zhang, W. W. Hong, Y. L. Jiang, W. Xu, H. L. Shuai, H. S. Hou and X. B. Ji, *J. Mater. Chem. A*, 2018, **6**, 11488–11495.

28 J. P. Paraknowitsch, A. Thomas and J. Schmidt, *Chem. Commun.*, 2011, **47**, 8283–8285.
29 N. Parveen, M. O. Ansari, S. A. Ansari and M. H. Cho, *J. Mater. Chem. A*, 2016, **4**, 233–240.
30 W. Q. Han, J. Cumings, X. S. Huang, K. Bradley and A. Zettl, *Chem. Phys. Lett.*, 2001, **346**, 368–372.
31 W. Kicinski, M. Szala and M. Bystrzejewski, *Carbon*, 2014, **68**, 1–32.
32 Z. Y. Wu, S. L. Xu, Q. Q. Yan, Z. Q. Chen, Y. W. Ding, C. Li, H. W. Liang and S. H. Yu, *Sci. Adv.*, 2018, **4**, eaat0788.
33 Z. S. Wu, Y. Z. Tan, S. Zheng, S. Wang, K. Parvez, J. Qin, X. Shi, C. Sun, X. Bao, X. Feng and K. Mullen, *J. Am. Chem. Soc.*, 2017, **139**, 4506–4512.
34 T. Yoshii, K. Chida, H. Nishihara and F. Tani, *Chem. Commun.*, 2022, **58**, 3578–3590.
35 H. Nishihara, T. Hirota, K. Matsuura, M. Ohwada, N. Hoshino, T. Akutagawa, T. Higuchi, H. Jinnai, Y. Koseki, H. Kasai, Y. Matsuo, J. Maruyama, Y. Hayasaka, H. Konaka, Y. Yamada, S. Yamaguchi, K. Kamiya, T. Kamimura, H. Nobukuni and F. Tani, *Nat. Commun.*, 2017, **8**, 109.
36 K. Chida, T. Yoshii, K. Takahashi, M. Yamamoto, K. Kanamaru, M. Ohwada, V. Deerattrakul, J. Maruyama, K. Kamiya, Y. Hayasaka, M. Inoue, F. Tani and H. Nishihara, *Chem. Commun.*, 2021, **57**, 6007–6010.
37 T. Ogoshi, Y. Sakatsume, K. Onishi, R. Tang, K. Takahashi, H. Nishihara, Y. Nishina, B. D. L. Campeon, T. Kakuta and T. A. Yamagishi, *Commun. Chem.*, 2021, **4**, 75.
38 K. Chida, T. Yoshii, N. Hiyoshi, T. Itoh, J. Maruyama, K. Kamiya, M. Inoue, F. Tani and H. Nishihara, *Carbon*, 2023, **201**, 338–346.
39 K. Chida, T. Yoshii, M. Ohwada, Y. Hayasaka, J. Komeda, R. Sakamoto, J. Maruyama, K. Kamiya, M. Inoue, F. Tani and H. Nishihara, *Catal. Today*, 2023, **411**, 113830.
40 R. S. Kathayat and N. S. Finney, *J. Am. Chem. Soc.*, 2013, **135**, 12612–12614.
41 L. Rocard, A. Berezin, F. De Leo and D. Bonifazi, *Angew. Chem., Int. Ed.*, 2015, **54**, 15739–15743.
42 S. Bernhardt, M. Kastler, V. Enkelmann, M. Baumgarten and K. Müllen, *Chem. – Eur. J.*, 2006, **12**, 6117–6128.
43 C. J. Sun, P. F. Wang, H. Wang and B. H. Han, *Polym. Chem.*, 2016, **7**, 5031–5038.
44 Y. R. Shi, M. A. Gerkman, Q. F. Qiu, S. R. Zhang and G. G. D. Han, *J. Mater. Chem. A*, 2021, **9**, 9798–9808.
45 S. T. Jackson and R. G. Nuzzo, *Appl. Surf. Sci.*, 1995, **90**, 195–203.
46 K. Kaneko and C. Ishii, *Colloids Surf.*, 1992, **67**, 203–212.
47 Z. Y. Ryu, J. T. Zheng, M. Z. Wang and B. J. Zhang, *Carbon*, 1999, **37**, 1257–1264.
48 Z. H. Hu, N. Maes and E. F. Vansant, *J. Porous Mater.*, 1995, **2**, 19–23.
49 M. Sadakane, K. Kodato, T. Kuranishi, Y. Nodasaka, K. Sugawara, N. Sakaguchi, T. Nagai, Y. Matsui and W. Ueda, *Angew. Chem., Int. Ed.*, 2008, **47**, 2493–2496.
50 K. Ma, L. Zhao, Z. Jiang, Y. Huang and X. Sun, *Polym. Compos.*, 2018, **39**, 1223–1233.
51 N. Hashimoto, K. Mori and H. Yamashita, *J. Phys. Chem. C*, 2023, **127**, 20786–20793.
52 M. J. Matthews, M. A. Pimenta, G. Dresselhaus, M. S. Dresselhaus and M. Endo, *Phys. Rev. B: Condens. Matter Mater. Phys.*, 1999, **59**, R6585–R6588.
53 Y. Guo, Z. Zeng, Y. Liu, Z. Huang, Y. Cui and J. Yang, *J. Mater. Chem. A*, 2018, **6**, 4055–4067.
54 G. Y. Zhao, D. F. Yu, H. Zhang, F. F. Sun, J. W. Li, L. Zhu, L. Sun, M. Yu, F. Besenbacher and Y. Sun, *Nano Energy*, 2020, **67**, 104219.
55 Y. Z. Su, Z. Q. Yao, F. Zhang, H. Wang, Z. Mics, E. Cánovas, M. Bonn, X. D. Zhuang and X. L. Feng, *Adv. Funct. Mater.*, 2016, **26**, 5893–5902.
56 H. J. Peng, V. Montes-Garcia, J. Raya, H. L. Wang, H. P. Guo, F. Richard, P. Samori and A. Ciesielski, *J. Mater. Chem. A*, 2023, **11**, 2718–2725.
57 A. Ivanovskaya, N. Singh, R. F. Liu, H. Kreutzer, J. Baltrusaitis, T. V. Nguyen, H. Metiu and E. McFarland, *Langmuir*, 2013, **29**, 480–492.
58 Z. G. Wang, P. J. Li, Y. F. Chen, J. R. He, W. L. Zhang, O. G. Schmidt and Y. R. Li, *Nanoscale*, 2014, **6**, 7281–7287.
59 L. Qie, W. M. Chen, X. Q. Xiong, C. C. Hu, F. Zou, P. Hu and Y. H. Huang, *Adv. Sci.*, 2015, **2**, 1500195.
60 W. Zhong, X. S. Lv, Q. W. Chen, M. M. Ren, W. L. Liu, G. D. Li, J. X. Yu, M. Li, Y. Dai and L. Z. Wang, *ACS Appl. Mater. Interfaces*, 2019, **11**, 37850–37858.
61 Q. Q. Wang, X. F. Ge, J. Y. Xu, Y. C. Du, X. Zhao, L. Si and X. S. Zhou, *ACS Appl. Energy Mater.*, 2018, **1**, 6638–6645.
62 H. M. Cui, J. G. Xu, J. S. Shi and C. Zhang, *J. CO2 Util.*, 2021, **50**, 101582.
63 S. Louisia, R. C. Contreras, M. Heitzmann, M. R. Axet, P. A. Jacques and P. Serp, *Catal. Commun.*, 2018, **109**, 65–70.
64 J. Y. Tian, Z. M. Liu, Z. H. Li, W. G. Wang and H. Y. Zhang, *RSC Adv.*, 2017, **7**, 12089–12097.
65 L. P. Wang, W. S. Jia, X. F. Liu, J. Z. Li and M. M. Titirici, *J. Energy Chem.*, 2016, **25**, 566–570.
66 S. Sfaelou, X. D. Zhuang, X. L. Feng and P. Lianos, *RSC Adv.*, 2015, **5**, 27953–27963.
67 Y. P. Guo, Z. Q. Zeng, Y. J. Liu, Z. G. Huang, Y. Cui and J. Y. Yang, *J. Mater. Chem. A*, 2018, **6**, 4055–4067.
68 R. Kamai, K. Kamiya, K. Hashimoto and S. Nakanishi, *Angew. Chem.*, 2016, **128**, 13378–13382.
69 Q. Q. Yan, D. X. Wu, S. Q. Chu, Z. Q. Chen, Y. Lin, M. X. Chen, J. Zhang, X. J. Wu and H. W. Liang, *Nat. Commun.*, 2019, **10**, 4977.
70 J. Liu, M. G. Jiao, L. L. Lu, H. M. Barkholtz, Y. P. Li, Y. Wang, L. H. Jiang, Z. J. Wu, D. J. Liu, L. Zhuang, C. Ma, J. Zeng, B. S. Zhang, D. S. Su, P. Song, W. Xing, W. L. Xu, Y. Wang, Z. Jiang and G. Q. Sun, *Nat. Commun.*, 2017, **8**, 15938.
71 H. Funke, A. C. Scheinost and M. Chukalina, *Phys. Rev. B: Condens. Matter Mater. Phys.*, 2005, **71**, 094110.